

Cite this: *J. Mater. Chem. A*, 2017, 5, 15124

## Effects of organic cations on the defect physics of tin halide perovskites†

Tingting Shi,<sup>a</sup> Hai-Shan Zhang,<sup>b</sup> Weiwei Meng,<sup>c</sup> Qiang Teng,<sup>b</sup> Meiyue Liu,<sup>ad</sup> Xiaobao Yang,<sup>ab</sup> Yanfa Yan,<sup>c</sup> Hin-Lap Yip<sup>\*ad</sup> and Yu-Jun Zhao<sup>\*ab</sup>

Tin (Sn) halide perovskite absorbers have attracted much interest because of their nontoxicity as compared to their lead (Pb) halide perovskite counterparts. Recent progress shows that the power conversion efficiency of FASnI<sub>3</sub> (FA = HC(NH<sub>2</sub>)<sub>2</sub>) solar cells prevails over that of MASnI<sub>3</sub> (MA = CH<sub>3</sub>NH<sub>2</sub>). In this paper, we show that the organic cations, *i.e.*, FA and MA, play a vital role in the defect properties of Sn halide perovskites. The antibonding coupling between Sn-5s and I-5p is clearly weaker in FASnI<sub>3</sub> than in MASnI<sub>3</sub> due to the larger ionic size of FA, leading to higher formation energies of Sn vacancies in FASnI<sub>3</sub>. Subsequently, the conductivity of FASnI<sub>3</sub> can be tuned from p-type to intrinsic by varying the growth conditions of the perovskite semiconductor; in contrast, MASnI<sub>3</sub> shows unipolar high p-type conductivity independent of the growth conditions. This provides a reasonable explanation for the better performance of FASnI<sub>3</sub>-based solar cells in experiments with respect to the MASnI<sub>3</sub>-based solar cells.

Received 27th March 2017  
Accepted 19th June 2017

DOI: 10.1039/c7ta02662e

rsc.li/materials-a

### 1. Introduction

The power conversion efficiency (PCE) of methylammonium lead tri-halide perovskite solar cells (PVSCs) has skyrocketed from less than 5% to over 22%,<sup>1–11</sup> in the past few years, due to the extraordinary optoelectronic properties of perovskite semiconductors.<sup>12–14</sup> The possibility for fabricating PVSCs using low cost solution processes makes them an even more appealing photovoltaic technology. Considering the broad applications and commercialization, a key scientific challenge is to replace the toxic Pb in the perovskite absorber with nontoxic elements, such as Sn, Ge, *etc.* In 2014, Kanatzidis's group and Snaith's group independently demonstrated methylammonium tin iodide (MASnI<sub>3</sub>, MA = CH<sub>3</sub>NH<sub>2</sub>) based Pb-free PVSCs with PCEs of around 6%.<sup>15,16</sup> However, very limited progress based on the MASnI<sub>3</sub> system has been made over the past two years probably due to the instability and poor reproducibility of the material. Recently, formamidinium tin iodide (FASnI<sub>3</sub>, FA = HC(NH<sub>2</sub>)<sub>2</sub>) based Pb-free perovskite solar cells have started to attract further attention,<sup>17,18</sup> with Yan's group reporting efficient

FASnI<sub>3</sub>-based solar cells with a PCE of up to 6.22% and much better device reproducibility.<sup>19</sup> Nevertheless, there were very limited studies dedicated to understanding the intrinsic difference of the material properties between FASnI<sub>3</sub> and MASnI<sub>3</sub>,<sup>20–26</sup> which is critically important to further improve the performance of the Pb-free perovskite solar cells.

One important approach to provide better insights into the material properties of perovskites is through theoretical investigation.<sup>27–29</sup> In 2014, Wei's group studied the defect properties of inorganic Pb-free perovskite semiconductor CsSnI<sub>3</sub> and depicted the influence of defects and synthesis conditions on the photovoltaic performance.<sup>27</sup> They found that due to the strong Sn 5s–I 5p antibonding coupling, Sn vacancies have very low formation energies in CsSnI<sub>3</sub>, leading to a very high concentration of Sn vacancies and therefore high p-type conductivity, regardless of the growth conditions. As a consequence, CsSnI<sub>3</sub> behaves like a conductor, rather than a semiconductor, limiting its application for photovoltaic devices. To our surprise, similar calculations had not been applied for comparing the defect properties of the MASnI<sub>3</sub> and FASnI<sub>3</sub> semiconductors despite that these systems were widely used for device demonstrations.

Therefore, in this letter, we study theoretically the defect properties of the two Pb-free Sn-based organic–inorganic perovskites, FASnI<sub>3</sub> and MASnI<sub>3</sub>. We reveal that the larger ionic size of FA weakens the antibonding coupling between Sn-5s and I-5p as compared to MA. This leads to lower formation energies of Sn vacancies in FASnI<sub>3</sub> than those in MASnI<sub>3</sub>, and thus results in a much smaller hole density in the FASnI<sub>3</sub> system in comparison with that in MASnI<sub>3</sub>. We find that the conductivity of FASnI<sub>3</sub> can be tuned from p-type to intrinsic by varying the

<sup>a</sup>School of Materials Science and Engineering, South China University of Technology, Guangzhou, Guangdong 510640, China. E-mail: msttshi@scut.edu.cn; msangusyip@scut.edu.cn; zhaoyj@scut.edu.cn

<sup>b</sup>Department of Physics, South China University of Technology, Guangzhou, Guangdong 510640, China

<sup>c</sup>Department of Physics and Astronomy, Wright Center for Photovoltaics Innovation and Commercialization, The University of Toledo, Toledo, Ohio 43606, USA

<sup>d</sup>State Key Laboratory of Luminescent Materials and Devices, South China University of Technology, Guangzhou, Guangdong 510640, China

† Electronic supplementary information (ESI) available. See DOI: 10.1039/c7ta02662e

growth conditions. Meanwhile,  $\text{MASnI}_3$  shows a unipolar p-type conductivity with very high hole densities, which is unfavorable for efficient solar cell applications. These results explain the experimental observations that  $\text{FASnI}_3$ -based solar cells generally perform better than  $\text{MASnI}_3$ -based solar cells.

## II. Theoretical methods

The electronic structure calculations of the Sn-based perovskites,  $\text{MASnI}_3$  and  $\text{FASnI}_3$  were performed based on the density functional theory (DFT) calculations using the Vienna ab initio simulation package (VASP) code<sup>30</sup> with the standard frozen-core projector augmented-wave (PAW) method.<sup>31,32</sup> The generalized gradient approximation (GGA) of Perdew–Burke–Ernzerhof (PBE)<sup>33</sup> functional is employed for the exchange–correlation potential. The cut-off energy for basis functions is 400 eV and the  $k$ -point mesh was obtained using the Monkhorst–Pack<sup>34</sup> method with a reasonable grid density. The defect calculations are based on a  $(3 \times 3 \times 3)$  or  $(3 \times 2 \times 2)$  supercell with a single G point. The lattices of supercells with defects are fixed based on the optimized primitive cell. Atoms are fully relaxed until the Hellmann–Feynman forces on them are within  $0.05 \text{ eV \AA}^{-1}$ . The energy difference per atom between the calculations with 400 eV and 500 eV cutoff energies is less than 2 meV. Moreover, the lattice changes are within 1% for the primitive cell when the cutoff energy changes from 400 eV to 500 eV. Projected crystal orbital Hamilton population (pCOHP) curves are calculated using the computer program LOBSTER (Local-Orbital Basis Suite Towards Electronic-Structure Reconstruction), which enables chemical-bonding analysis based on the periodic plane-wave DFT output.<sup>35–37</sup>

For defect calculations, more accurate functionals are preferred in general, for example, the Heyd–Scuseria–Ernzerhof hybrid functional with the spin–orbit coupling (HSE–SOC) would be better.<sup>38,39</sup> Practically, however, HSE and HSE–SOC calculations are very time consuming and show a similar high defect tolerance in perovskites.<sup>38</sup> For  $\text{FASnI}_3$ , our PBE calculated bandgap (1.19 eV) is only slightly narrower than the experimental bandgap of 1.4 eV.<sup>19</sup> The PBE calculations of  $\text{FASnI}_3$  with SOC and without SOC are depicted in Fig. 1S† for showing the small change of bandgap values which is 0.21 eV, unlike the

situation in Pb-based perovskites.<sup>40</sup> So the PBE–SOC calculated bandgap is 0.98 eV, which is 0.42 eV smaller than the experimental bandgap. Fortunately, we found later that the doping properties are mainly determined by the shallow defects, such as Sn vacancies, MA or FA vacancies, I vacancies, MA or FA interstitials. The shallow defect levels typically shift with the band edges whose characteristics will not be changed with and without SOC.

The transition and formation energies<sup>41</sup> of intrinsic defects were calculated by equations below

$$\varepsilon(0/q) = [\varepsilon_{\text{D}}^{\Gamma}(0) - \varepsilon_{\text{VBM}}^{\Gamma}(\text{host})] + [E(\alpha, q) - (E(\alpha, q) - q\varepsilon_{\text{D}}^{\text{S}}(0))]/(-q) \quad (1)$$

$$\Delta H_{\text{f}}(\alpha, q) = \Delta E(\alpha, q) + \sum n_i \mu_i + qE_{\text{F}} \quad (2)$$

Here  $\varepsilon(0/q)$  is the transition energy,  $\Delta H_{\text{f}}$  is the defect formation energy, and  $E(\alpha, q)$  is the total energy for a supercell containing a defect  $\alpha$  in a charge state of  $q$ . The formation energy also depends on the atomic chemical potentials  $\mu_i$  and the electron Fermi energy  $E_{\text{F}}$ .

## III. Results and discussion

$\text{FASnI}_3$  has an orthorhombic ( $Amm2$ ) crystal structure,<sup>19</sup> and  $\text{MASnI}_3$  has a pseudocubic crystal ( $P4mm$ ) structure.<sup>15</sup> Both structures are established on the basic octahedral Sn–I framework. Fig. 1(a) shows the atomic structure of  $\text{FASnI}_3$ , with the white, red and light blue ones representing the organic FA molecule, I atom, and Sn atom respectively. The calculated band structure of the  $\text{FASnI}_3$  system is depicted in Fig. 1(b) showing a direct band gap value of 1.19 eV, which is in line with the experimental value (1.4 eV).<sup>19</sup> In the Pb halide perovskite systems, the unique s–p antibonding coupling contributes significantly to their remarkable optoelectronic properties. In the Sn-based systems, obvious Sn–5s and I–5p antibonding was also formed at the VBM, which is indicated by the charge distribution in Fig. 1(c).

Considering the thermodynamic equilibrium conditions, the existence of  $\text{FASnI}_3$  should satisfy

$$\mu_{\text{FA}} + \mu_{\text{Sn}} + 3\mu_{\text{I}} = \Delta H_{\text{f}}(\text{FASnI}_3) = -4.67 \text{ eV} \quad (3)$$

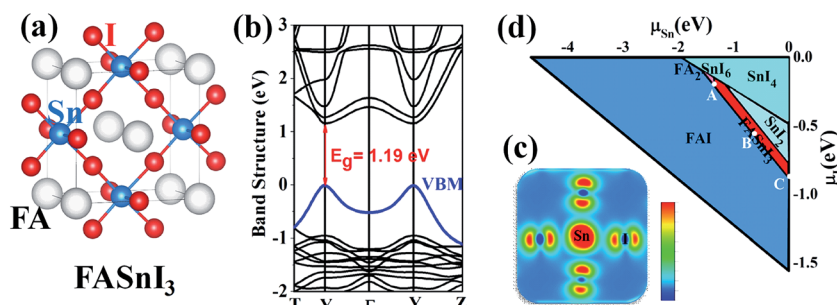


Fig. 1 (a) The schematic perovskite structure of  $\text{FASnI}_3$ , (b) band structure of  $\text{FASnI}_3$ , (c) partial charge density at the VBM, (d) thermodynamically stable range for equilibrium growth of  $\text{FASnI}_3$  and three typical chemical environments, marked by A, B and C.

where  $\mu_i$  ( $i = \text{FA}, \text{Sn}, \text{and I}$ ) is the chemical potential of the constituent element referring to its most stable phase and  $\Delta H_f(\text{FASnI}_3)$  is the formation enthalpy of  $\text{FASnI}_3$ . For  $\mu_{\text{FA}}$ , we choose a body-centered-cubic phase of FA which was also found in the Cs counterpart. To exclude the possible secondary phases of  $\text{SnI}_2$ ,  $\text{SnI}_4$ , FAI (rock-salt phase) and  $\text{FA}_2\text{SnI}_6$ , the following constraints must also be satisfied:

$$\mu_{\text{FA}} + \mu_{\text{I}} < \Delta H_f(\text{FAI}) = -2.91 \text{ eV} \quad (4)$$

$$\mu_{\text{Sn}} + 2\mu_{\text{I}} < \Delta H_f(\text{SnI}_2) = -1.55 \text{ eV} \quad (5)$$

$$\mu_{\text{Sn}} + 4\mu_{\text{I}} < \Delta H_f(\text{SnI}_4) = -1.94 \text{ eV} \quad (6)$$

$$2\mu_{\text{FA}} + \mu_{\text{Sn}} + 6\mu_{\text{I}} < \Delta H_f(\text{FA}_2\text{SnI}_6) = -7.98 \text{ eV} \quad (7)$$

The chemical potentials of Sn and I satisfying eqn (3)–(7) are shown as the red region in Fig. 1(d). Different from the Pb-based system, the narrow chemical range will be cut off partially by the competing  $\text{SnI}_4$  and  $\text{FA}_2\text{SnI}_6$  phases. The narrow red chemical range indicates that the growth conditions for synthesizing the  $\text{FASnI}_3$  phase should be carefully controlled, which is also indicated by the small dissociation energy of 0.21 eV of  $\text{FASnI}_3$  to FAI and  $\text{SnI}_2$ .

To evaluate how the organic cations may affect the defect properties, we have calculated the transition energies and formation energies of the most possible intrinsic point defects, including FA, Sn, and I vacancies ( $V_{\text{FA}}$ ,  $V_{\text{Sn}}$ , and  $V_{\text{I}}$ ), FA, Sn and I interstitials ( $\text{FA}_i$ ,  $\text{Sn}_i$ , and  $\text{I}_i$ ), FA on Sn and Sn on FA cation substitutions ( $\text{FA}_{\text{Sn}}$  and  $\text{Sn}_{\text{FA}}$ ) and four antisite substitutions, FA on I ( $\text{FA}_i$ ), Sn on I ( $\text{Sn}_i$ ), I on FA ( $\text{I}_{\text{FA}}$ ), and I on Sn ( $\text{I}_{\text{Sn}}$ ). The transition energies of these twelve defects are shown in Fig. 2S(a) (see ESI†). Since the formation energies of point defects depend on the chemical potentials of the constituent elements, we have chosen three typical points, labeled A (I-rich/Sn-poor), B (moderate) and C (I-poor/Sn-rich), in the chemical range shown in Fig. 1(d). The formation energies of the considered point defects as a function of the Fermi level position at chemical potential point A, B, and C are shown in

Fig. 2(a), (b) and (c), respectively. At point A or B,  $\text{FASnI}_3$  shows good *p*-type characteristics due to the dominant acceptor  $V_{\text{Sn}}$  with the lowest formation energy. At point C,  $\text{FASnI}_3$  should be an intrinsic (low conductivity) semiconductor as the dominant donor  $\text{FA}_i$  will compensate for acceptor  $V_{\text{Sn}}$  and the Fermi level will be pinned at the middle location of the band gap, pointed out by the black arrow in Fig. 2(c). These results indicated that the conductivity of  $\text{FASnI}_3$  strongly depends on the growth conditions and it is possible to tune its conductivity by choosing the desired growth conditions. In  $\text{FASnI}_3$ , the dominant donor  $\text{FA}_i$  and dominant acceptors  $V_{\text{Sn}}$  have comparable formation energies. The low formation energy of  $V_{\text{Sn}}$  in  $\text{FASnI}_3$  is due to the energetically unfavorable s–p antibonding coupling, which resembles the s–p antibonding coupling in  $\text{MAPbI}_3$  (ref. 42) and the p–d antibonding coupling in  $\text{CuInSe}$ .<sup>43</sup> The fully occupied antibonding state between Sn-5s and I-5p coupling does not gain energy significantly and thus tends to break a weak bond and easily forms a vacancy. The lower formation energy of  $\text{FA}_i$  could be expected due to the weak van der Waals interaction formed between the organic molecule FA and the Sn–I framework.

However, the situation in the  $\text{MASnI}_3$  system is different. We have calculated the twelve intrinsic defects in analogy with  $\text{FASnI}_3$ , including three vacancies  $V_{\text{MA}}$ ,  $V_{\text{Sn}}$ , and  $V_{\text{I}}$ , three interstitial defects  $\text{MA}_i$ ,  $\text{Sn}_i$ , and  $\text{I}_i$  and six substitutions  $\text{MA}_{\text{Sn}}$ ,  $\text{Sn}_{\text{MA}}$ ,  $\text{FA}_i$ ,  $\text{Sn}_i$ ,  $\text{I}_{\text{FA}}$  and  $\text{I}_{\text{Sn}}$  (see Fig. 2S(b), ESI†). The small dissociation energy of  $\text{MASnI}_3$  to MAI and  $\text{SnI}_2$  is 0.23 eV. Here we also have chosen three typical growth conditions with different chemical potentials similar to the case in the  $\text{FASnI}_3$  model, point A still represents the I-rich/Sn-poor environment, B is the moderate one, and C represents the I-poor/Sn-rich environment indicated by Fig. 3S (ESI†). No matter how the chemical potential is varied,  $V_{\text{Sn}}$  is the invariable dominant defect under different growth conditions, with the lowest formation energy across the whole Fermi energy range as shown in Fig. 3(a)–(c). Such a phenomenon could be attributed to the energetically unfavorable s–p antibonding coupling, which leads to the low formation energies of Sn vacancies in the

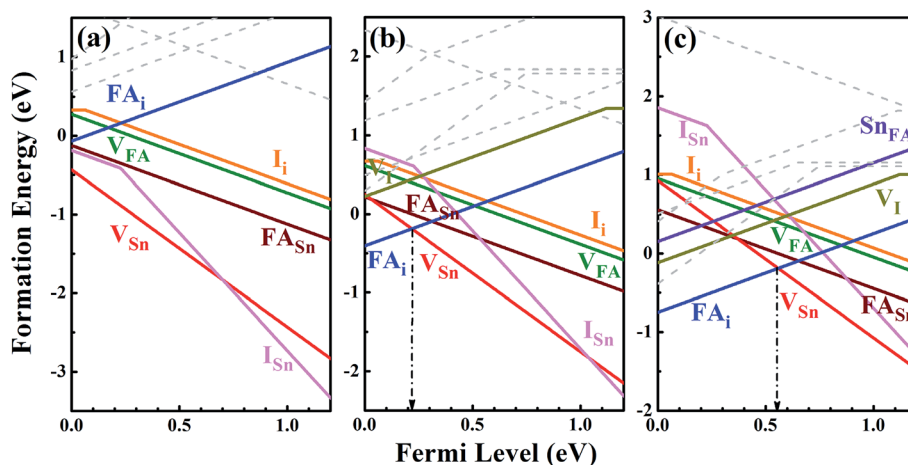


Fig. 2 The formation energies of intrinsic point defects in  $\text{FASnI}_3$  under different chemical potential conditions A (a), B (b), and C (c) shown in Fig. 1(d). Gray dashed lines represent the remaining defects with high formation energies.

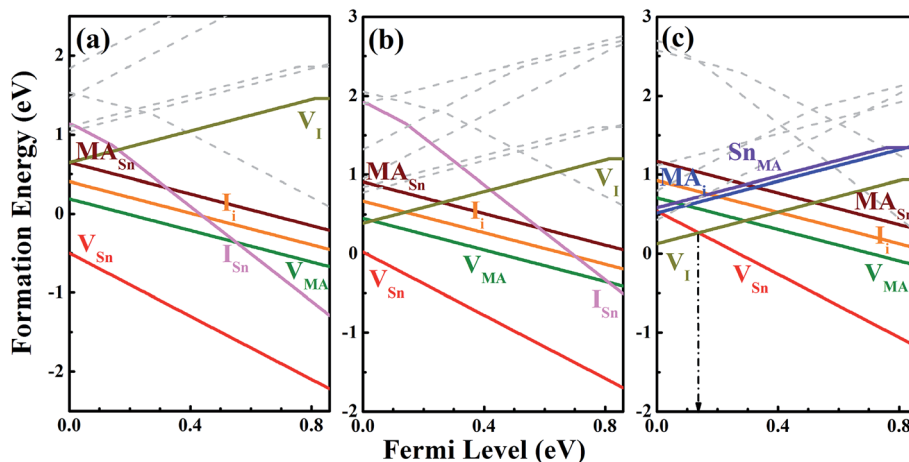


Fig. 3 The formation energies of intrinsic point defects in  $\text{MASnI}_3$  at different chemical potential A (a) I-rich/Sn-poor condition, B (b) moderate condition and C (c) I-poor/Sn-rich condition. Gray dashed lines represent the remaining defects with high formation energies.

$\text{MASnI}_3$  system. Under the I-poor/Sn-rich condition C, we also found that the defect  $\text{V}_I$  could be formed easily, which becomes a dominant defect in the wide Fermi level region. Therefore, the stronger s-p antibonding coupling in  $\text{MASnI}_3$ , compared with that in  $\text{FASnI}_3$ , leads to invariably the lowest formation energies of Sn vacancies in  $\text{MASnI}_3$ .<sup>44</sup>

For the Pb-free Sn-based perovskite systems, the VBM is also derived from the I-5p and Sn-5s orbitals. The coupling strength will finally determine the energy position of the VBM. The average Sn-I bond length is 3.31 Å in  $\text{FASnI}_3$ , which is longer than that of 3.23 Å in  $\text{MASnI}_3$ . As mentioned above, the shorter bond length will result in stronger anti-bonding coupling, which leads to an increase of the VBM of  $\text{MASnI}_3$  to a higher

energy level in comparison with that in  $\text{FASnI}_3$ . Furthermore, in order to provide a better picture on the distribution of electronic states in the two Sn-based systems, their partial densities of states (PDOSs) were calculated and are shown in Fig. 4. After aligning the I-5p levels, indicated by the grey arrow, it is clearly seen that the upper Sn-5s level is higher in energy in  $\text{FASnI}_3$  than in  $\text{MASnI}_3$ . The fact that the Sn-5s orbital energy in  $\text{MASnI}_3$  is higher than that in  $\text{FASnI}_3$  is consistent with the average Sn-I bond lengths in  $\text{FASnI}_3$  and  $\text{MASnI}_3$ , mainly due to the smaller size of the MA molecule, as compared with FA. Consequently, the  $\text{V}_{\text{Sn}}$  defects will have relatively lower formation energies in  $\text{MASnI}_3$  than in  $\text{FASnI}_3$  under similar growth conditions.

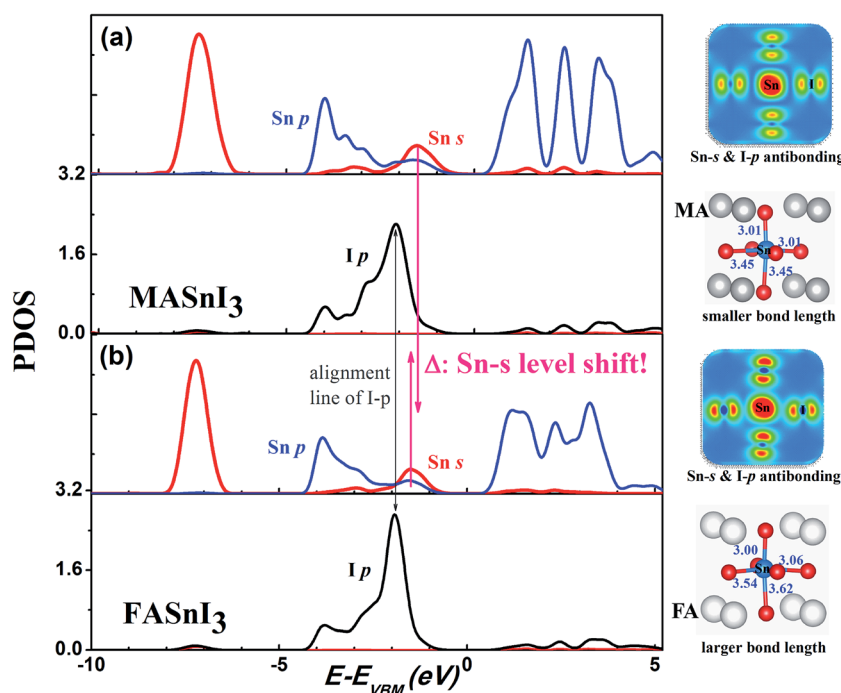


Fig. 4 Partial DOS of Sn and I, the corresponding bond lengths and the partial charge density around the VBM in  $\text{MASnI}_3$  (a) and in  $\text{FASnI}_3$  (b).

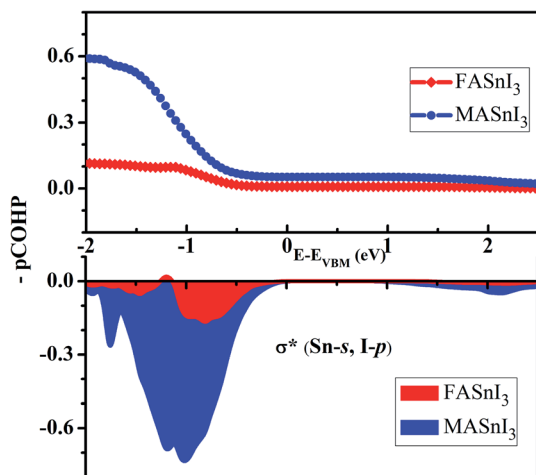


Fig. 5 Bonding analysis of Sn-5s, I-5p in FASnI<sub>3</sub> and MASnI<sub>3</sub> around the VBM within the energy range [ $E_{\text{VBM}} - 2$  eV,  $E_{\text{VBM}} + 2.5$  eV], using pCOHP based on PAW results by VASP processed with LOBSTER.

The difference of antibonding coupling in FASnI<sub>3</sub> and MASnI<sub>3</sub> has been depicted qualitatively according to the comparison of their electronic properties. To take one step further, we also performed quantitative analysis based on the  $-p\text{COHP}$  calculation, which had been used to analyze the chemical bonding/antibonding type and bonding strength<sup>45,46</sup> and applied in perovskite systems.<sup>28,46</sup> Here the energy window from  $E_{\text{VBM}} - 2$  eV to  $E_{\text{VBM}} + 2.5$  eV is set to compare the bonding of Sn-5s and I-5p around the VBM. The blue line and the blue area represent the  $-p\text{COHP}$  of MASnI<sub>3</sub> and its integration, respectively, while the red ones represent those of the FASnI<sub>3</sub>. Obviously, the orbital overlap population of MASnI<sub>3</sub> is much higher than the one of FASnI<sub>3</sub> shown in Fig. 5, which further emphasizes the weaker antibonding coupling of Sn-5s and I-5p in FASnI<sub>3</sub>.

## IV. Conclusion

With a theoretical investigation of intrinsic defects of FASnI<sub>3</sub> and MASnI<sub>3</sub> under possible growth conditions, we reveal that the semiconductor nature of FASnI<sub>3</sub> can be tuned from p-type to intrinsic by changing the growth conditions, while MASnI<sub>3</sub> shows a unipolar p-type characteristic with very high hole density. This explains the experimental observations of a better PCE performance of FASnI<sub>3</sub>-based solar cells with respect to the MASnI<sub>3</sub>-based one. Furthermore, we found that the higher formation energy of Sn vacancies in FASnI<sub>3</sub> is mainly due to the weaker Sn-5s and I-5p antibonding coupling originating from the larger size of FA and longer bond length of Sn-I, which suggests that composition engineering of Sn-based perovskites would be an important strategy to improve the physical properties of the material.

## Acknowledgements

This work is supported by the NSFC (Grant 11574088, 51431001, 51573057 and 21761132001), the Fundamental Research Funds

for the Central Universities (Grant 2015ZP010, 2015PT017) and the China Postdoctoral Science Foundation (Grant 2017M612646). The computer times at the National Supercomputing Center in Guangzhou (NSCCGZ) are gratefully acknowledged. T. S. also acknowledges the discussion with Dr Zhaoning Song and Prof. Pengyi Liu (Guangzhou Key Laboratory of Vacuum Coating Technologies and New Energy Materials, 201605030008).

## References

- M. A. Green, K. Emery, Y. Hishikawa, W. Warta, E. D. Dunlop, D. H. Levi and A. W. Y. Ho-Baillie, *Prog. Photovoltaics Res. Appl.*, 2017, **25**, 3–13.
- <http://www.nrel.gov/pv/assets/images/efficiency-chart.png>.
- J. H. Im, C. R. Lee, J. W. Lee, S. W. Park and N. G. Park, *Nanoscale*, 2011, **3**, 4088–4093.
- M. M. Lee, J. Teuscher, T. Miyasaka, N. T. Murakami and H. J. Snaith, *Science*, 2011, **338**, 643.
- H. S. Kim, C. R. Lee, J. H. Im, K. B. Lee, T. Moehl, A. Marchioro, S. J. Moon, R. H. Baker, J. H. Yum, J. E. Moser, M. Grätzel and N. G. Park, *Sci. Rep.*, 2012, **2**, 591.
- J. Burschka, N. Pellet, S.-J. Moon, R. Humphry-Baker, P. Gao, M. K. Nazeeruddin and M. Grätzel, *Nature*, 2013, **499**, 316–319.
- D. Liu and T. L. Kelly, *Nat. Photonics*, 2013, **8**, 133–138.
- M. Liu, M. B. Johnston and H. J. Snaith, *Nature*, 2013, **501**, 395–398.
- J. H. Noh, S. H. Im, J. H. Heo, T. N. Mandal and S. I. Seok, *Nano Lett.*, 2013, **13**, 1764–1769.
- W. S. Yang, J. H. Noh, N. J. Jeon, Y. C. Kim, S. Ryu, J. Seo and S. Seok, *Science*, 2015, **348**, 1234–1237.
- A. Guerrero, J. You, C. Aranda, Y. S. Kang, G. Garcia-Belmonte, H. Zhou, J. Bisquert and Y. Yang, *ACS Nano*, 2016, **10**, 218–224.
- G. Xing, N. Mathews, S. Sun, S. S. Lim, Y. M. Lam, M. Grätzel, S. Mhaisalkar and T. C. Sum, *Science*, 2014, **342**, 344.
- W. J. Yin, T. Shi and Y. Yan, *Adv. Mater.*, 2014, **26**, 4653–4658.
- S. D. Stranks, G. E. Eperon, G. Grancini, C. Menelaou, M. J. P. Alcocer, T. Leijtens, L. M. Herz, A. Petrozza and H. J. Snaith, *Science*, 2014, **342**, 341.
- F. Hao, C. C. Stoumpos, R. P. Chang and M. G. Kanatzidis, *J. Am. Chem. Soc.*, 2014, **136**, 8094–8099.
- N. K. Noel, S. D. Stranks, A. Abate, C. Wehrenfennig, S. Guarnera, A. Haghighirad, A. Sadhanala, G. E. Eperon, S. K. Pathak, M. B. Johnston, A. Petrozza, L. M. Herz and H. J. Snaith, *Energy Environ. Sci.*, 2014, **7**, 3061.
- S. J. Lee, S. S. Shin, Y. C. Kim, D. Kim, T. K. Ahn, J. H. Noh, J. Seo and S. I. Seok, *J. Am. Chem. Soc.*, 2016, **138**, 3974–3977.
- F. Wang, J. Ma, F. Xie, L. Li, J. Chen, J. Fan and N. Zhao, *Adv. Funct. Mater.*, 2016, **26**, 3417–3423.
- W. Liao, D. Zhao, Y. Yu, R. C. Grice, C. Wang, A. Cimaroli, P. Schulz, W. Meng, K. Zhu, R. G. Xiong and Y. Yan, *Adv. Mater.*, 2016, **28**, 9333–9340.
- W. Liao, D. Zhao, Y. Yu, R. C. Grice, C. Wang, A. Cimaroli, P. Schulz, W. Meng, K. Zhu, R. G. Xiong and Y. Yan, *J. Am. Chem. Soc.*, 2016, **138**, 12360–12363.

- 21 M. H. Kumar, S. Dharani, W. L. Leong, P. P. Boix, R. R. Prabhakar, T. Baikie, C. Shi, H. Ding, R. Ramesh, M. Asta, M. Grätzel, S. G. Mhaisalkar and N. Mathews, *Adv. Mater.*, 2014, **26**, 7122–7127.
- 22 H.-J. Du, W.-C. Wang and J.-Z. Zhu, *Chin. Phys. B*, 2016, **25**, 108802.
- 23 M.-C. Jung, S. R. Raga and Y. Qi, *RSC Adv.*, 2016, **6**, 2819–2825.
- 24 S. J. Lee, S. S. Shin, Y. C. Kim, D. Kim, T. K. Ahn, J. H. Noh, J. Seo and S. I. Seok, *J. Am. Chem. Soc.*, 2016, **138**, 3974–3977.
- 25 T. Yokoyama, D. H. Cao, C. C. Stoumpos, T. B. Song, Y. Sato, S. Aramaki and M. G. Kanatzidis, *J. Phys. Chem. Lett.*, 2016, **7**, 776–782.
- 26 M. Zhang, M. Lyu, J.-H. Yun, M. Noori, X. Zhou, N. A. Cooling, Q. Wang, H. Yu, P. C. Dastoor and L. Wang, *Nano Res.*, 2016, **9**, 1570–1577.
- 27 P. Xu, S. Chen, H.-J. Xiang, X.-G. Gong and S.-H. Wei, *Chem. Mater.*, 2014, **26**, 6068–6072.
- 28 D. Yang, J. Lv, X. Zhao, Q. Xu, Y. Fu, Y. Zhan, A. Zunger and L. Zhang, *Chem. Mater.*, 2017, **29**, 524–538.
- 29 Y. He and G. Galli, *Chem. Mater.*, 2014, **26**, 5394–5400.
- 30 G. Kresse and J. Hafner, *Phys. Rev. B: Condens. Matter Mater. Phys.*, 1993, **47**, 558–561.
- 31 P. E. Blöchl, *Phys. Rev. B: Condens. Matter Mater. Phys.*, 1994, **50**, 17953–17979.
- 32 G. Kresse and D. Joubert, *Phys. Rev. B: Condens. Matter Mater. Phys.*, 1999, **59**, 1758–1775.
- 33 J. P. Perdew, K. Burke and E. Matthias, *Phys. Rev. Lett.*, 1996, **77**, 3865–3868.
- 34 H. J. Monkhorst and J. D. Pack, *Phys. Rev. B: Condens. Matter Mater. Phys.*, 1976, **13**, 5188–5192.
- 35 V. L. Deringer, A. L. Tchougreff and R. Dronskowski, *J. Phys. Chem. A*, 2011, **115**, 5461–5466.
- 36 S. Maintz, V. L. Deringer, A. L. Tchougreff and R. Dronskowski, *J. Comput. Chem.*, 2016, **37**, 1030–1035.
- 37 <http://schmeling.ac.rwth-aachen.de/cohp/index.php?menuID=6>.
- 38 J. Kang and L. W. Wang, *J. Phys. Chem. Lett.*, 2017, **8**, 489–493.
- 39 J. Heyd, G. E. Scuseria and M. Ernzerhof, *J. Chem. Phys.*, 2003, **118**, 8207–8215.
- 40 M. H. Du, *J. Phys. Chem. Lett.*, 2015, **6**, 1461–1466.
- 41 Y. Yan and S.-H. Wei, *Phys. Status Solidi B*, 2008, **245**, 641–652.
- 42 W.-J. Yin, T. Shi and Y. Yan, *Appl. Phys. Lett.*, 2014, **104**, 063903.
- 43 S. B. Zhang, S.-H. Wei, A. Zunger and H. Katayama-Yoshida, *Phys. Rev. B: Condens. Matter Mater. Phys.*, 1998, **57**, 9642.
- 44 Note: we notice that the formation energies of Sn vacancies are negative in the whole Fermi energy range at point A (I-rich/Sn-poor) for both FASnI<sub>3</sub> and MASnI<sub>3</sub> (cf. Fig. 2(a) and 3(a)) are unphysical, and it is attributed to some unknown competing defected phases of ternaries although we have taken FA<sub>2</sub>SnI<sub>6</sub>, MA<sub>2</sub>SnI<sub>6</sub> and SnI<sub>4</sub> into consideration. The relative formation energy of Sn vacancies in FASnI<sub>3</sub> and MASnI<sub>3</sub>, as well as the main conclusions of the letter, will not be affected by further refinement of the stable chemical potential ranges.
- 45 M. Kupers, P. Konze, S. Maintz, S. Steinberg, A. Mio, O. Cojocar-Miredin, M. Zhu, M. Muller, M. Luysberg, J. Mayer, M. Wuttig and R. Dronskowski, *Angew. Chem.*, 2017, **56**, 1–6.
- 46 Q. Fu, J. L. Li, T. He and G. W. Yang, *J. Appl. Phys.*, 2013, **113**, 104303.